Spectroscopy and nuclear dynamics of starburst galaxies

Vermaas, L.

3

The nuclear dynamics of Arp 220

L. Vermaas and P. P. van der Werf

Abstract

We present high-resolution K-band integral field spectroscopy of the nearby Ultraluminous Infrared galaxy Arp 220. The observations provide a detailed view of the nuclear stellar and nebular emission, and allow determinations of both the gas and stellar velocity field, providing independent probes of the dynamical mass. While the stellar emission and the Brγ emission show the two nuclei, the H_2 emission is dominated by a large-scale regularly rotating disk. The stellar velocity field shows that the nuclei are counter-rotating with respect to each other, in agreement with the nuclear gas components as measured from higher resolution CO data. The stellar velocity dispersion does not reveal any peaks. The total dynamical mass of the stellar nuclei is $M_{*,\mathrm{tot}} = (1.2 \pm 0.4) \cdot 10^{10} M_{\odot}$, where the error is dominated by the uncertainty in the effective radii. This value is in excellent agreement with the dynamical mass within 0.6 kpc determined from the H_2 velocity field, which is $M_{\mathrm{tot}} = (1.2 \pm 0.6) \cdot 10^{10} M_{\odot}$, where the uncertainty is dominated by the uncertainty in the inclination of the disk. We find that the molecular gas, with a mass of $5 \times 10^9 M_{\odot}$ constitutes a significant fraction of the dynamical mass. The K-band stellar mass to light ratio, corrected for extinction is $M/L_K \sim 0.05$, with at least a factor of two uncertainty resulting from the uncertainty in the extinction correction. Even taking these uncertainties into account, this value indicates an important starburst contribution to the nuclear K-band emission.

3.1 Introduction

The galaxy Arp 220 is the closest ultraluminous infrared galaxy (ULIRG), with a luminosity distance $D_{\rm L} = 77\,{\rm Mpc}$ (using a flat cosmology with $H_0 = 73\,{\rm km\,s^{-1}\,Mpc^{-1}}$, $\Omega_{\rm b} = 0.27$ and $\Omega_\Lambda = 0.73$, so that $1''$=400 pc) and an infrared luminosity (defined as the luminosity between 8 and 1000 μm in the rest frame) $L_{\rm IR} = 1.5 \cdot 10^{12}\,L_\odot$ (Sanders et al. 2003). It was the first galaxy identified as a ULIRG from the IRAS survey (Soifer et al. 1984). It shows a double nucleus at near-infrared (Graham et al. 1990, Scoville et al. 1998), mid-infrared (Soifer et al. 1999), (sub)millimetre (Scoville et al. 1997, Sakamoto et al. 1999, Downes & Eckart 2007, Sakamoto et al. 2008, Aalto et al. 2009, Matsushita et al. 2009) and radio (Norris 1988, Rodríguez-Rico et al. 2005) wavelengths, with a projected nuclear separation $0\farcs95 \approx 0.36\,{\rm kpc}$. Tidal tails have been detected in the optical regime (Joseph & Wright 1985). This galaxy, like ULIRGs in general, is thus in a final stage of merging and has a large concentration of gas in its centre. The nuclear region harbours an OH megamaser (Baan et al. 1982, Lonsdale et al. 1998, Rovilos et al. 2003) and also displays H_2CO megamaser emission (Baan et al. 1986, 1993, Baan & Haschick 1995, Araya et al. 2004). The molecular gas component in the nuclear region is extraordinarily concentrated: Scoville et al. (1991) estimated an average molecular gas density of $2900\,{\rm cm^{-3}}$ and surface density of $8 \times 10^4\,M_\odot\,{\rm pc^{-2}}$. Observations of density tracing molecules such as CS, HCN and HCO^+ indicate that the bulk of the molecular gas is dense (Solomon et al. 1990) with densities in the range of $10^{5-6}\,{\rm cm^{-3}}$ (Greve et al. 2009, Papadopoulos et al. 2010a,b).

Scoville et al. (1997) first showed two compact sources in CO $J = 1-0$ and dust continuum observations, embedded in an extended disk-like component of approximately a kpc in diameter. This was confirmed by Downes & Solomon (1998), who estimated the total gas mass within the central region to be approximately $5 \cdot 10^9\,M_\odot$, of which 90% is located in the nuclear region within a radius of 600 pc (including both nuclei). The gas mass of the western nucleus was estimated to be $1 \cdot 10^9\,M_\odot$, while that for the eastern nucleus was $6 \cdot 10^8\,M_\odot$. Similar gas masses were found from CO $J = 2-1$ imaging at $0\farcs5$ resolution by Sakamoto et al. (1999), who found the gaseous disks in the two nuclei to counter-rotate, which is also observed in HI absorption observations (Mundell et al. 2001).

The origin of the infrared luminosity, intense star formation or a significant contribution from an Active Galactic Nucleus (AGN), has been debated for decades. The relative faintness of hydrogen recombination lines such as Br γ has been used to argue in favour of an obscured AGN (Rieke et al. 1985), but as shown by van der Werf (2001), this is naturally expected in a starburst dominated by compact HII regions, where a large fraction of UV photons is absorbed by dust, so that starburst analysis based on standard (dust-free) photoionization models is yields incorrect results. The presence of intense star formation in the nuclei is shown directly by radio VLBI measurements, which resolve the radio emission from the two nuclei into large numbers of radio supernova remnants (Smith et al. 1998, Rovilos et al. 2005, Lonsdale et al. 2006, Parra et al. 2007), and through radio recombination lines from the nuclei (Zhao et al. 1996, Anantharamaiah et al. 2000, Rodríguez-Rico et al. 2005). Optical studies of the Arp 220 stellar system also reveal a young stellar population and massive young super star clusters (Shaya et al. 1994, Shioya et al. 2001a, Wilson et al. 2006, Rodríguez Zaurín

et al. 2008). Models to account for these properties also point towards a strongly obscured nuclear starburst (Shioya et al. 2001b). There is also a prominent optical superwind and X-ray (Heckman et al. 1987, 1996, Arribas et al. 2001, McDowell et al. 2003, Colina et al. 2004), presumably powered by this starburst. The question is therefore not whether a starburst is present in Arp 220, but whether it is the only power source. Hard X-ray and soft γ-ray observations failed to provide direct evidence for an AGN (Dermer et al. 1997, Iwasawa et al. 2001, Clements et al. 2002, Iwasawa et al. 2005), but an AGN hidden by a column density of at least $5 \cdot 10^{24}\,\mathrm{cm}^{-2}$ cannot be ruled out. Very large amounts of extinction towards the source of luminosity, irrespective of its nature, are certainly indicated by observations in the mid-infrared (Spoon et al. 2004, 2007). The fact that even mid-infrared tracers show no high-excitation lines that could betray the presence of a hidden AGN (Genzel et al. 1998, Imanishi & Dudley 2000, Imanishi et al. 2006, Armus et al. 2007, Imanishi et al. 2007, Farrah et al. 2007, Risaliti et al. 2010).

Early near-IR spectra of Arp 220 (Rieke et al. 1985, Goldader et al. 1995) showed prominent H_2 2.12 μm emission lines, and early images of the Paβ and [Fe II] near-IR J-band lines were presented by Armus et al. (1995b). Near-IR long slit spectroscopy of Arp 220 in the H and K-bands was presented first by Armus et al. (1995a) and Larkin et al. (1995). The latter authors showed that that hydrogen recombination lines (Paβ, Brγ) in Arp 220 are associated with the near-IR nuclei, while the H_2 rovibrational 2.12 μm line and [Fe II] have a significant part of their flux in between. They also suggested that H_2 and [Fe II] are also kinematically decoupled from Paβ and Brγ.

The near-infrared K-band offers the opportunity for simultaneously measuring gas kinematics (from various emission lines) and stellar kinematics (from sharp stellar photospheric absorption features). The first analysis of stellar kinematics in Arp 220 using photospheric features in the K-band was done by Doyon et al. (1994) using long slit spectroscopy, resulting in a stellar velocity dispersion $\sigma_* = 150 \pm 21\,\mathrm{km\,s}^{-1}$. The same technique was used in a series of much more comprehensive and sensitive studies of significant samples of ULIRGs and and QSOs (Genzel et al. 2001, Tacconi et al. 2002, Dasyra et al. 2006a,b). These studies indicated that the stellar dynamics of ULIRGs is dominated by random motions, but that rotation is often important as well. Pre-merging ULIRGs were found to be major mergers where in most cases the merging galaxies have similar masses, and the end products of the mergers were found to be moderate mass ellipticals.

The advent of near-IR integral field spectroscopy enables a new step forwards in this field. Where slit observations can be affected by kinematic misalignments, integral field data allow a clean separation of rotation and dispersion over the field. The high resolution afforded by adaptive optics is an additional advantage that minimises beam smearing and allows accurate measurements of velocity dispersion even in the presence of strong velocity gradients. A final advantage of near-IR integral field spectroscopy is the presence of nebular emission lines, that provide an independent probe of the gravitational potential (e.g., Neumayer et al. 2007, Cappellari et al. 2009). In order to fully explore this method, we here present and analyse adaptive-optics assisted near-IR integral field spectroscopy of Arp 220.

Table 3.1 – K-band continuum and line fluxes in both nuclei, measured in a rectangular region of $1\farcs0 \times 1\farcs25$ (see section 3.3.1). Errors in the fluxes are typically 10%.

	$F_{\rm east}$	$F_{\rm west}$	
K cont (λ_c=2.2μm)	$1.65 \cdot 10^{-12}$	$2.01 \cdot 10^{-12}$	erg s^{-1}cm$^{-2}\mu$m^{-1}
H_2 (2.12μm)	$37.5 \cdot 10^{-16}$	$42.6 \cdot 10^{-16}$	erg s^{-1}cm^{-2}
Brγ (2.17μm)	$18.1 \cdot 10^{-16}$	$15.2 \cdot 10^{-16}$	erg s^{-1}cm^{-2}
Brδ (1.95μm)	$7.8 \cdot 10^{-16}$	$8.5 \cdot 10^{-16}$	erg s^{-1}cm^{-2}

3.2 Observations and data reduction

The central region of Arp 220 was observed with SINFONI, the Spectrograph for INtegral Field Observations in the Near Infrared (1.1 - 2.45 μm), which is installed on UT4 of the VLT (Eisenhauer et al. 2003, Bonnet et al. 2004). The observations were carried out in the night of July 19, 2009. The Laser Guide Star was used for Adaptive Optics. Tip/tilt correction was attempted on the optical galaxy, but due to its faintness it does not provide a strong correction. The intermediate platescale was used, with a field of view of $3'' \times 3''$ onto 64×64 spatial pixels. Each of these pixels is projected onto 2218 spectral elements in the K-band, with a central wavelength of 2.2μm. This results in spatial pixels with a resolution of $0\farcs05 \times 0\farcs10$, and a spectral resolution $\lambda/\Delta\lambda$ of 4000.

The nuclear separation of Arp 220 is about $1''$, so with this setup both nuclei and their surroundings can be observed in one field. For the pointings, an ABA$'$ nodding mode was used, i.e. object-sky-object with equal integration times of 900 s, with the A' frame slightly shifted with respect to the A frame. The total (on-source) integration time was 5×900 s, or 75 minutes.

The data were reduced with the SINFONI pipeline, version 2.0.5, which was developed by ESO and the Max-Planck-Institut für extraterrestrische Physik. The default procedure included corrections for non-linearity, distortion and wavelength calibration.

For both flux calibration and telluric feature removal, a standard star was observed with the same setup as used for the science frames, typically an early type star containing few stellar lines in the near-IR. After standard reduction, the average stellar spectrum was extracted and the photospheric stellar lines were removed (Brγ). Finally, each spectrum of the reduced object frame was divided by this extracted spectrum. The size of the point spread function (PSF) is estimated to be $0\farcs4$ (150 pc); this fairly large PSF results from the lack of a suitably bright tip-tilt star.

3.3 Results

The continuum was determined by linear interpolation of the broad-band spectra, emission lines were fitted with single Gaussians in each pixel. The resulting maps of the K-band continuum, Brγ and the rovibrational H_2 (2.12 μm) line emission are shown in Fig. 3.1. The

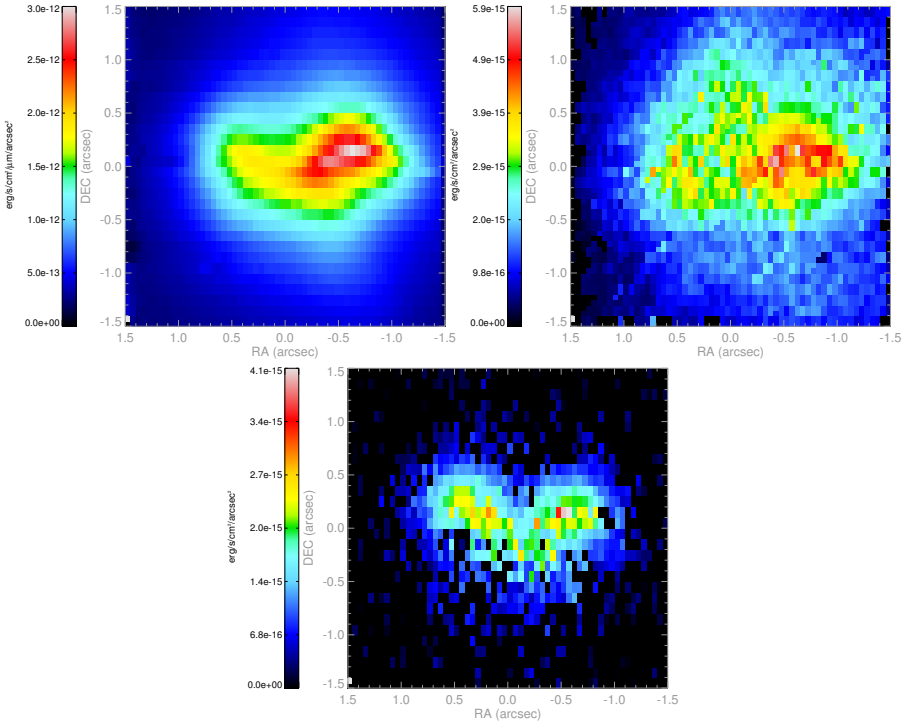

Figure 3.1 – SINFONI flux maps of K band continuum (left), H_2 2.12 μm (middle) and Brγ 2.17 μm (right). The location (0,0) in these images is set to the pointing position of the observation, RA: 15h 34m 57.2s; DEC: +23d 30m 11.5s. East is left and north is up.

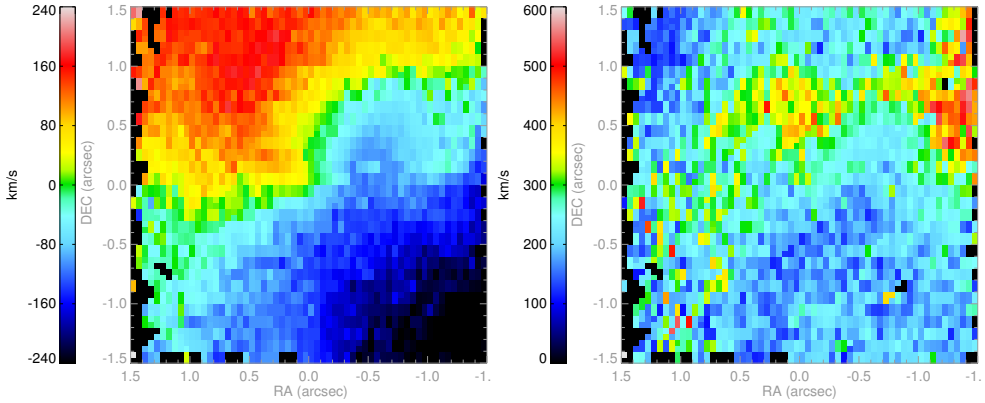

Figure 3.2 – H_2 velocity (left) and velocity dispersion (right). The systemic velocity has been set to 5434 km/s. The location (0,0) denotes the pointing position of observation, as in Fig. 3.1.

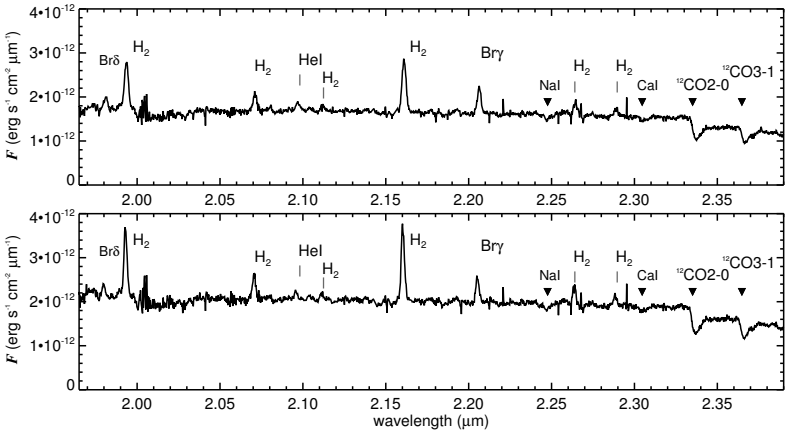

Figure 3.3 – Integrated K-band spectra of the east (left) and west (right) nucleus, from rectangular boxes of $1\farcs0 \times 1\farcs25$ centred on the nuclear positions. Central coordinates in Fig. 3.1 of east spectrum: (0.3,0.0); of west spectrum: (−0.7,0.05).

K-band continuum has a shape in which the original two nuclei are recognised. However, the right (western) peak clearly dominates the NIR continuum. The H_2 emission at 2.12 μm follows this shape and also peaks on the western nucleus, while the Br γ line map shows equal contributions from both nuclei.

3.3.1 Spectra

The K-band spectra (Fig. 3.3) of the east and west nucleus are quite similar. Both spectra were integrated in a rectangular region of $1\farcs0 \times 1\farcs25$, centred on the nuclear positions: (0.3,0.0) for the east nucleus and (−0.7,0.05) for the west nucleus, using the coordinates of Fig. 3.1. The recombination lines Br γ, Br δ and He I are comparable in strength in both nuclei. However, the level of the *K*-band continuum as well as the strength of the excited H_2 lines is higher in the west nucleus. Stellar absorption features of Na I (2.21μm), Ca I (2.26μm), and CO (^{12}CO 2−0 at 2.29μm and ^{13}CO 2−0 at 2.34μm) are recognised in both, and these are slightly narrower in the western nucleus.

3.3.2 Gas kinematics

The H_2 (2.12 μm) velocity field is shown in the left frame of Fig. 3.2. The gas velocity field is dominated by large scale, almost regular rotation. Closer inspection reveals signatures associated with the two nuclei, which may reflect the local effect of the nuclear gravitational potentials, but these features are much weaker than the overall rotation. The H_2 velocity dispersion (Fig. 3.2, right) shows two relatively shallow peaks that are not directly related to the nuclei.

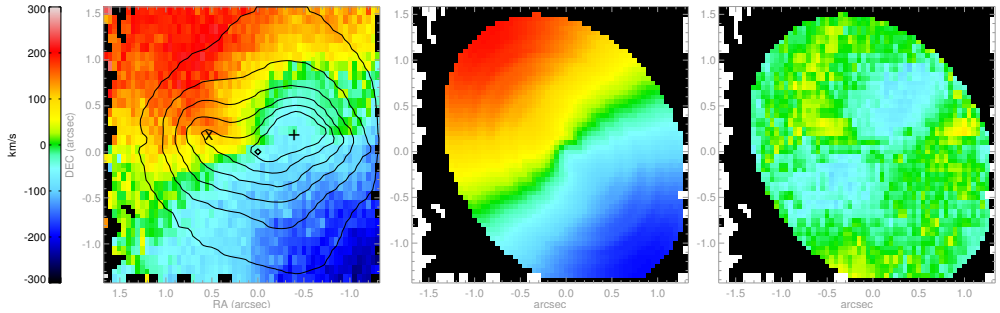

Figure 3.4 – Left: original H_2 velocity field (v_{orig}). X marks the location of the east nucleus, + marks the west nucleus and the diamond (◇) marks the kinematic centre of the Kinemetry-model. Centre: Circular H_2 velocity field (v_{circ}), resulting from the tilted ring model. Right: residual velocity field (v_{res}=v_{orig}-v_{circ}). All images have the same colour scale, and (0,0) is the location of the kinematic centre.

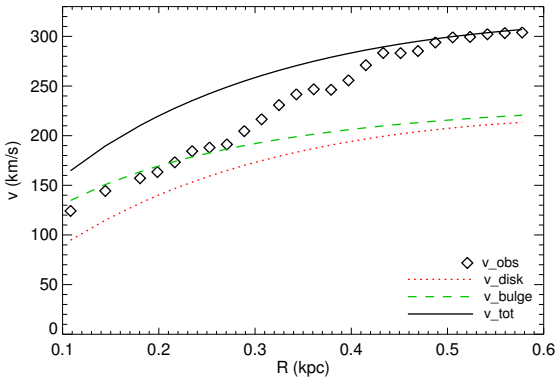

Figure 3.5 – Rotation curve of H_2, resulting from the tilted ring model fit described in the text, out to 0.6 kpc along the major axis. The open diamonds indicate the observed points, while fitted disk, bulge and total mass model are shown by the red dotted line, dashed green line and drawn black line respectively. The fit was constrained to reproduce the observed rotation curve at large radii.

The H_2 velocity field was fitted with a set of tilted rings, using the IDL-based code Kinemetry (Krajnović et al. 2006). The kinematic centre position was fixed at the centre of the outer K-band isophotes, which roughly corresponds to the point in between the maximum and minimum velocities. This location matches the kinematic centre in the CO velocity field of Downes & Solomon (1998). Tilted rings were fitted at increasing radii (r), with position angle (PA) as free parameter, and inclination (i) fixed to 40°, following the inclination of the CO-disk (Downes & Solomon 1998, Eckart & Downes 2001). Fig. 3.4 shows the original H_2 velocity field, now with (0,0) at the kinematic centre (left), the fitted circular velocity field (v_{circ}, middle) and the residual velocity field (v_{res}=v_{orig}-v_{circ}, right). The velocity field is dominated by the large scale rotation of a gas disk, instead of the rotation of the nuclei themselves, as opposed to for instance high resolution CO observations by Sakamoto et al.

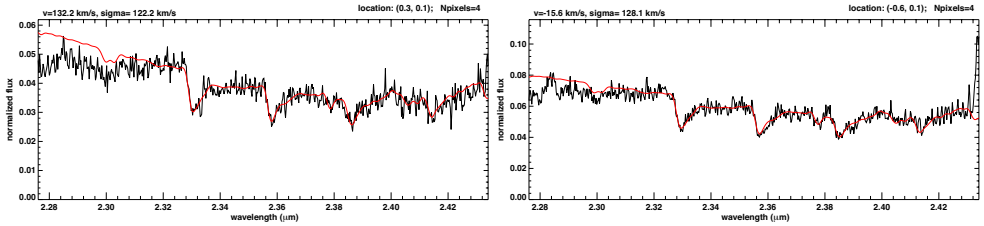

Figure 3.6 – Part of the K-band spectrum with absorption features (black), with the PPXF-fit with 6 template spectra overplotted (red). Left: east nucleus. Right: west nucleus. Note that the strong CO bands are well matched, as well as several other stellar absorption features.

(1999), who did find significant rotation of the nuclei separately in the CO gas. We do see some rotation that is associated with the nuclei in the residuals, but it is clear that its signature is unimportant compared to the large scale structure of the nuclear velocity field, which can be modelled as a simple rotating disk.

The central rotation curve of H_2 resulting from our tilted ring fit is shown in Fig. 3.5. The inner part rises linearly (solid body rotation), and bends at 0.5 kpc, although the point where the rotation curve will flatten cannot be exactly determined from these data. The PSF size is small compared to the scale of the rotation curve, so the slow rising of the curve is real and is not a result of beam smearing.

3.3.3 Stellar kinematics

The stellar absorption features of CO (^{12}CO 2-0 at 2.29μm and ^{12}CO 3-1 at 2.32μm) were fitted with 6 stellar template spectra of different spectral types, which originated from SINFONI observations as well. For this fit we used Penalised Pixel Fitting (PPXF) from Cappellari & Emsellem (2004). Before the fitting, the spatial pixels were combined according to the Voronoi method, and in our case a S/N of 20 for each bin was sufficient for high quality fits in order to obtain a coherent stellar velocity field. Fitted spectra at the nuclear locations are shown in Fig 3.6. The resulting stellar velocity field and velocity dispersion field are shown in Fig. 3.7, left and right respectively. The (formal) errors in the fit of the velocity dispersion are typically 10-20 km/s in most of the bins, except the large bins in the outer parts where the error is larger.

3.3.4 Velocity profiles

Contrary to the situation with the gas, the stellar kinematics shows quite clearly the rotation of the two nuclei. The stellar velocity fields in the two nuclei actually match well the velocity fields derived from high resolution CO observations Sakamoto et al. (1999, 2008). Cuts in stellar velocity and velocity dispersion through the two nuclei are shown in Fig. 3.8. This figure also shows the velocity profiles of Brγ and H_2 in these same cuts. The cuts are centred on the infrared nuclei (pixels of maximum flux) and the position angles are chosen along

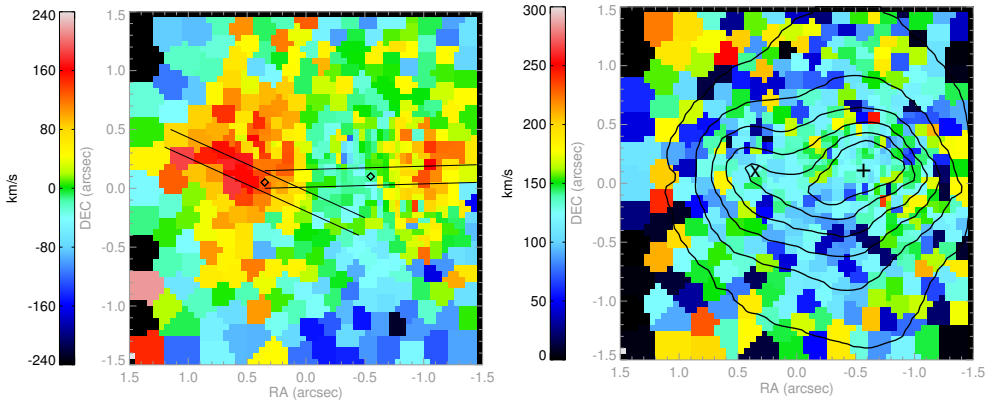

Figure 3.7 – Left: stellar velocity field, with profile cut positions. Right: stellar velocity dispersion, with K-band continuum contours.

highest stellar velocity gradient. The orientations of both cuts are shown in Fig. 3.7 (right). The velocity profiles of the Brγ and H_2 gas match quite well. The profiles of stellar velocity deviate from the gas, especially in the western nucleus, and these deviations are due to the fact that H_2 and Brγ trace the large-scale rotation at central gas disk, while the stellar kinematics is dominated by the two nuclei. This result also implies that a dominant part of the ionised gas (Brγ) is taking part in the dynamics of the large-scale gas disk, even though the Brγ flux distribution peaks at the positions of the two nuclei (Engel et al. 2011).

The rotation of the stellar system as a whole, outside the nuclear region, is slower than the rotation of the gas. Therefore, the stellar system must to a large extent be dynamically supported by random motions. The stellar velocity dispersion is essentially constant: no peak is seen in either of the nuclei, nor between the nuclei at the centre of the weaker isophotes, and the measured velocity dispersion is $\sigma_* = 130 \pm 10\,\mathrm{km\,s^{-1}}$. This value is within the error bars compatible with the early value $\sigma_* = 151 \pm 25\,\mathrm{km\,s^{-1}}$ measured by Doyon et al. (1994). A somewhat higher velocity dispersion $\sigma_* = 165 \pm 10\,\mathrm{km\,s^{-1}}$ was found by Genzel et al. (2001) using single slits. The discrepancy with our data may arise from the uncertainties of separating rotation and random motions in single slit data. A much larger velocity dispersion of 275 to 300 km s^{-1} is found by Engel et al. (2011). This value is absolutely ruled out by our results, as can be seen easily from Fig. 3.6. We note however that the results by Engel et al. (2011) were obtained using the lower resolution $R \approx 1500$ H+K grating of SINFONI. Their data therefore do not have sufficient spectral resolution for resolving the stellar kinematics, and we adopt here our own measurement $\sigma_* = 130 \pm 10\,\mathrm{km\,s}-1$ as the best measurement of the stellar velocity dispersion.

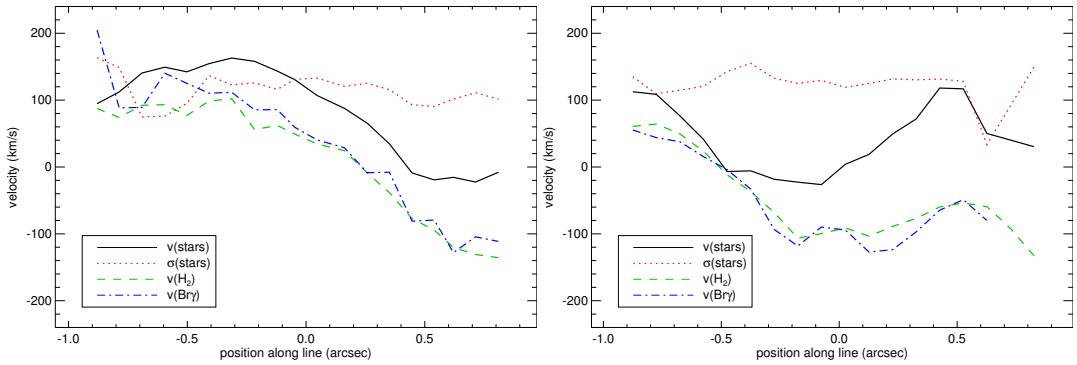

Figure 3.8 – Left: velocity profiles through the east nucleus. Right: velocity profiles through the west nucleus. Positions of the profile cuts are indicated in Fig. 3.7, right-hand panel.

3.4 Discussion: nuclear dynamics

In this section, we will first use the stellar dynamics to determine the mass of the near infrared nuclei. Then we will discuss the gas dynamics by taking the H_2 rotation curve (section 3.3.2 and us it to make a model of the mass. Consequently, we will discuss the importance of the gas and stellar components for the nuclear dynamics of Arp 220.

3.4.1 Mass estimate from stellar kinematics

For a non-rotating stellar system, the dynamical mass M_* can be calculated from the expression

$$\frac{M_*}{M_\odot} = 1.4 \cdot 10^6 \left(\frac{\sigma_*}{\mathrm{km\,s^{-1}}}\right)^2 \frac{R_{\mathrm{eff}}}{\mathrm{kpc}}, \tag{3.1}$$

where σ_* is the stellar velocity dispersion and R_{eff} is the effective radius (i.e., the radius enclosing half the total light). This equation is an application of the general expression in Bender et al. (1992, their Eq. (3)), and the numerical factor in this equation depends on he adopted mass distribution. The factor $1.4 \cdot 10^6$ results from a constant M/L King model with $R_{\mathrm{tidal}}/R_{\mathrm{core}} = 50$, an appropriate choice of parameters for spheroids between a dwarf and a giant elliptical (Bender et al. 1992, see Appendix A of), following Tacconi et al. (2002) and Dasyra et al. (2006b). For a spherical system, this formula can be modified to include the effects of rotational support by adopting the expression

$$\frac{M_*}{M_\odot} = 4.7 \cdot 10^5 \left[3\left(\frac{\sigma_*}{\mathrm{km\,s^{-1}}}\right)^2 + \left(\frac{v_*}{\mathrm{km\,s^{-1}}}\right)^2\right] \frac{R_{\mathrm{eff}}}{\mathrm{kpc}}, \tag{3.2}$$

where v_* is the stellar rotational velocity at radius R_{eff} (Appendix B of Bender et al. 1992, Dasyra et al. 2006b).

For R_{eff}, Scoville et al. (2000) give 0.58 kpc for Arp 220 as a whole. Genzel et al. (2001) use this result to adopt values 0.6 ± 0.3 kpc for each of the two nuclei, but since the distance

between the nuclei is only 0.36 kpc, this approach is not tenable. While the nuclei do not show a peak in velocity dispersion, they do show considerable rotation, and the measured rotation velocity is $v_* = 90 \pm 10\,\mathrm{km\,s^{-1}}$ for the eastern nucleus and $v_* = 70 \pm 10\,\mathrm{km\,s^{-1}}$ for the western nucleus. The rotation patterns can be traced out to a radius of $\sim 0\farcs5$ (0.2 kpc) from the centre of each nucleus. The nuclei may actually be somewhat more extended, but beyond this radius their light is no longer dominant over the larger scale host galaxy. We therefore adopt the value $R_{\mathrm{eff}} = 0.2 \pm 0.1$ kpc for each of the two nuclei. Since the stellar velocity fields match very well the velocity fields derived from high resolution CO data for the two nuclei Sakamoto et al. (1999, 2008), we can use the inclinations derived from the CO data. For the western nucleus, Engel et al. (2011) give $i \approx 50^\circ$ based on the CO data, where we estimate the error $\Delta i \approx 10^\circ$. For the eastern nucleus, Engel et al. (2011) could not derive an inclination from the CO data, so we follow these authors and adopt $i \approx 50 \pm 25^\circ$. The inclination-corrected stellar rotation velocities are then $90^{+20}_{-10}\,\mathrm{km\,s^{-1}}$ and $120^{+100}_{-25}\,\mathrm{km\,s^{-1}}$ for the western and eastern nucleus. The implied dynamical masses are $M_* = (5.7 \pm 3.0) \cdot 10^9\,M_\odot$ for the western nucleus and $M_* = (6.0 \pm 3.0) \cdot 10^9\,M_\odot$ for the eastern nucleus, within a 0.2 kpc radius for both. The total dynamical mass of the two nuclei is then $M_{*,\mathrm{tot}} = (1.2 \pm 0.4) \cdot 10^{10}\,M_\odot$.

3.4.2 Mass estimate from gas kinematics

The H_2 rotation curve (Fig. 3.5) rises slowly, thus suggesting that there is no dominant central concentration in the distribution of stellar and gas mass. Only a mass concentration smaller than our PSF ($0.4''$ or 150 pc) could be hidden by beam smearing in our velocity field, but this would manifest itself as a peak in the gas velocity dispersion, which is not observed. Of course local mass concentrations do exist in the form of the two nuclei, but these have only subtle effects on the local H_2 velocity field. CO observations clearly reveal the nuclei in the molecular gas velocity field, and the absence of signatures of the nuclei in the present data is most likely due to significant nuclear extinction (see Sect. 3.4.3). The fact that these nuclei are separated by a significant distance, so that their mass is effectively spread over a much larger volume than the combined volumes of the nuclei themselves, may be responsible for the slowly rising rotation curve. We note that the flux distribution of H_2 is quite smooth, no clear peaks are observed so that there is no reason to assume a central concentration of gas, unless it is selectively extincted. Nevertheless, these considerations show that it is difficult to model the inner part of the H_2 rotation curve accurately, in spite of its regular appearance. In order to model the mass distribution giving rise to the H_2 rotation curve we therefore focus on the outer parts of the rotation curve only, which is relatively insensitive to the precise distribution of mass close to the kinematic centre. In order to have sufficient freedom in our mass model we adopt a combination of a disk and bulge. The bulge has a Hernquist profile (Hernquist 1990) with characteristic radius $a = R_{\mathrm{eff}}/(1+\sqrt{2})$ and total mass M_{bulge} as free parameters. The disk parameters, scale length h and central surface brightness Σ_0, are not entirely free but in combination satisfy the condition that the gas mass within the region is approximately $5 \cdot 10^9\,M_\odot$ (Downes & Solomon 1998, Sakamoto et al. 2008). We imported the inclination corrected H_2 gas rotation curve into GIPSY (the Groningen Image Processing SYstem, van der Hulst et al. 1992, Vogelaar & Terlouw 2001) and used the procedure

ROTMAS. The resulting mass model, considering only the outer points of the rotation curve, is shown in Fig. 3.5. The resulting mass model consists of a disk with a mass, by construction, of $M_{\rm disk} = 5 \cdot 10^9\,M_\odot$ (with $\Sigma_0 = 1.3 \cdot 10^4\,M_\odot\,{\rm pc}^{-2}$ and $h = 0.35\,{\rm kpc}$) and a bulge with a mass $M_{\rm bulge} = 7 \cdot 10^9\,M_\odot$ ($R_{\rm eff} = 2.5\,{\rm kpc}$) within the a radius of 0.59 kpc, the outermost point on the rotation curve. The total mass within this region is then $M_{\rm tot} = (1.2 \pm 0.6) \cdot 10^{10}\,M_\odot$. Even when ignoring the gas mass condition, introducing a considerable freedom in how the total mass is apportioned between the model disk and model bulge, the total mass of the two is well determined (for instance, fitting only an exponential disk yields a result that is only 15% larger). Consequently, the error in the total mass is dominated by the uncertainty in the inclination of the disk, and this is the uncertainty quoted in our result. This mass determination, which considers radii out to 0.59 kpc is in excellent agreement with the mass determined for the two nuclei in Sect. 3.4, but there is sufficient error margin to include some additional mass for the host galaxy and the gas component. The mass of the gas disk in the nuclear region of Arp 220 of $5 \cdot 10^9\,M_\odot$ (Downes & Solomon 1998, Sakamoto et al. 2008) therefore forms a significant part of the total dynamical mass.

3.4.3 Mass to light ratio

We calculate the total K-band luminosity within a radius of 0.6 kpc to be $L_K = 1.8 \cdot 10^{10}\,L_{K,\odot}$, where we have used a solar absolute K-band magnitude of 3.28. Without extinction correction, the value of M/L_K is then $0.6 \pm 0.3\,M_\odot/L_{K,\odot}$. Since there is a good match between the flux distribution in Br γ and the K-band continuum, both can be extinction corrected using the ratio of hydrogen recombination lines and assuming the near-IR extinction curve of Martin & Whittet (1990). In the present case we use the pixel-by-pixel ratio of $F_{{\rm Br}\gamma}/F_{{\rm Br}\delta}$, which has an intrinsically constant value of 1.519 (Hummer & Storey 1987). The Br δ-line is detected with confidence over the whole nuclear region where we assume extinction is not negligible (e.g., Scoville et al. 2000). The extinction-corrected K-band luminosity in the same region is then $1.05 \cdot 10^{11}\,L_{K,\odot}$; in other words, 83% of the emitting K-band emission is absorbed, consistent with the analysis by Engel et al. (2011). In terms of an effective extinction integrated over the nuclei, we find $A_K = 1.9$ or $A_V = 17$, following Fitzpatrick (1999). The resulting extinction-corrected M/L_K is $0.11 \pm 0.5\,M_\odot/L_{K,\odot}$, over an area of 6.1 arcsec^2 or 0.82 kpc^2. Comparison with the synthetic starburst models of STARBURST99 (Leitherer et al. 1999, Vázquez & Leitherer 2005, Leitherer et al. 2010) shows that for an instantaneous burst of star formation, this M/L_K is reached at a time of about $1.8 \cdot 10^8$ years. In this model a power law stellar initial mass function (IMF) is used with a slope $\alpha = 2.35$ for stellar masses between 1 and $100\,M_\odot$. Comparisons with starburst models should be viewed with some caution, since a significant fraction of the nuclear light may represent older stars from the bulges of the progenitor nuclei, and the M/L_K of the starburst component alone is in general hard to determine. However, evolved populations have significantly higher values than observed here (e.g., Vázquez & Leitherer 2005), and the present measurements thus at least indicate an important starburst contribution.

The extinction derived here for the central region is significant but not extreme, and this result is in agreement with earlier extinction determinations for the nuclei (e.g., Scoville et al.

1998, Engel et al. 2011). We derive maximum values of $A_V \sim$45 in each of the nuclei. The central region of Arp 220 does harbour regions of very high column density (e.g., Scoville et al. 1991, Downes & Solomon 1998, Spoon et al. 2004, Sakamoto et al. 1999, Papadopoulos et al. 2010a,b), which could amount to $A_V \sim 1000$ if located in an absorbing foreground screen, and regions behind such a screen would be undetected in our data. In the context of this model, Scoville et al. (1998) have proposed that that the nuclei are intersected by totally opaque gas disks, which would completely hide 50% of the nuclear emission from view. Adopting this additional correction would provide an intrinsic $M/L_K \sim 0.05$. In terms of the starburst model referred to above, the implied age would then be 6×10^7 years. Clearly the quality of these estimates are very sensitive to the extent to which the extinction can be reliably corrected.

3.5 Conclusions

We have obtained high resolution near-IR *K*-band integral field spectroscopy of the nearby ULIRG Arp 220. The data provide a detailed view of the nuclear stellar and nebular emission and extinction, as well as of the velocity and velocity dispersion fields of both gas and stars. These independent velocity fields provide independent probes of the nuclear dynamical mass. We obtain the following results:

1. While the stellar emission and also the Brγ nebular emission reveal the two remnant nuclei, the H_2 emission reveals and extended disk, with little evidence of influence from the two nuclei.

2. The velocity field of the H_2 emission reveals a regularly rotating disk, with minor velocity distortions at the positions of the two nuclei.

3. In contrast, the stellar velocity field shows prominent rotation of the two nuclei, while little rotation is observed in the larger scale host galaxy. The two nuclei counter-rotate with respect to each other, but their rotation patterns agree with that derived from high resolution CO observations. The stellar velocity dispersion field does not reveal any prominent peaks.

4. Analysis of the nuclear stellar kinematics gives a total dynamical mass of $M_{*,\mathrm{tot}} = (1.2 \pm 0.4) \cdot 10^{10} M_\odot$ for the two nuclei together, where the error is dominated by the uncertainty in the effective radii.

5. The H_2 velocity field provides a dynamical mass within a radius of 0.6 kpc of $M_{\mathrm{tot}} = (1.2 \pm 0.6) \cdot 10^{10} M_\odot$, where the uncertainty is dominated by the uncertainty in the disk's inclination. The determinations from gas dynamics and stellar dynamics are in excellent agreement.

6. The molecular gas, with a mass of $5 \times 10^9 M_\odot$ constitutes a significant fraction of the dynamical mass.

7. The K-band stellar mass to light ratio, corrected for extinction and is $M/L_K \sim 0.05$, with at least a factor of two uncertainty resulting from the uncertainty in the extinction correction. Even taking these uncertainties into account, this value indicates an important starburst contribution to the nuclear K-band emission.

These results illustrate the power of high resolution near-IR integral field spectroscopy for analysing the nuclear starburst and the dynamical properties of the nuclear regions of ULIRGs in general.

References

Aalto, S., Wilner, D., Spaans, M., et al. 2009, A&A, 493, 481

Anantharamaiah, K. R., Viallefond, F., Mohan, N. R., Goss, W. M., & Zhao, J. H. 2000, ApJ, 537, 613

Araya, E., Baan, W. A., & Hofner, P. 2004, ApJS, 154, 541

Armus, L., Charmandaris, V., Bernard-Salas, J., et al. 2007, ApJ, 656, 148

Armus, L., Neugebauer, G., Soifer, B. T., & Matthews, K. 1995a, AJ, 110, 2610

Armus, L., Shupe, D. L., Matthews, K., Soifer, B. T., & Neugebauer, G. 1995b, ApJ, 440, 200

Arribas, S., Colina, L., & Clements, D. 2001, ApJ, 560, 160

Baan, W. A., Guesten, R., & Haschick, A. D. 1986, ApJ, 305, 830

Baan, W. A. & Haschick, A. D. 1995, ApJ, 454, 745

Baan, W. A., Haschick, A. D., & Uglesich, R. 1993, ApJ, 415, 140

Baan, W. A., Wood, P. A. D., & Haschick, A. D. 1982, ApJ, 260, L49

Bender, R., Burstein, D., & Faber, S. M. 1992, ApJ, 399, 462

Bonnet, H., Abuter, R., Baker, A., et al. 2004, The Messenger, 117, 17

Cappellari, M. & Emsellem, E. 2004, PASP, 116, 138

Cappellari, M., Neumayer, N., Reunanen, J., et al. 2009, MNRAS, 394, 660

Clements, D. L., McDowell, J. C., Shaked, S., et al. 2002, ApJ, 581, 974

Colina, L., Arribas, S., & Clements, D. 2004, ApJ, 602, 181

Dasyra, K. M., Tacconi, L. J., Davies, R. I., et al. 2006a, ApJ, 638, 745

Dasyra, K. M., Tacconi, L. J., Davies, R. I., et al. 2006b, ApJ, 651, 835

Dermer, C. D., Bland-Hawthorn, J., Chiang, J., & McNaron-Brown, K. 1997, ApJ, 484, L121+

Downes, D. & Eckart, A. 2007, A&A, 468, L57

Downes, D. & Solomon, P. M. 1998, ApJ, 507, 615

Doyon, R., Wells, M., Wright, G. S., et al. 1994, ApJ, 437, L23

Eckart, A. & Downes, D. 2001, ApJ, 551, 730

Eisenhauer, F., Abuter, R., Bickert, K., et al. 2003, in Presented at the Society of Photo-Optical Instrumentation Engineers (SPIE) Conference, Vol. 4841, Society of Photo-Optical Instrumentation Engineers (SPIE) Conference Series, ed. M. Iye & A. F. M. Moorwood, 1548–1561

Engel, H., Davies, R. I., Genzel, R., et al. 2011, ApJ, 729, 58

Farrah, D., Bernard-Salas, J., Spoon, H. W. W., et al. 2007, ApJ, 667, 149

Fitzpatrick, E. L. 1999, PASP, 111, 63

Genzel, R., Lutz, D., Sturm, E., et al. 1998, ApJ, 498, 579

Genzel, R., Tacconi, L. J., Rigopoulou, D., Lutz, D., & Tecza, M. 2001, ApJ, 563, 527

Goldader, J. D., Joseph, R. D., Doyon, R., & Sanders, D. B. 1995, ApJ, 444, 97

Graham, J. R., Carico, D. P., Matthews, K., et al. 1990, ApJ, 354, L5

Greve, T. R., Papadopoulos, P. P., Gao, Y., & Radford, S. J. E. 2009, ApJ, 692, 1432

Heckman, T. M., Armus, L., & Miley, G. K. 1987, AJ, 93, 276

Heckman, T. M., Dahlem, M., Eales, S. A., Fabbiano, G., & Weaver, K. 1996, ApJ, 457, 616

Hernquist, L. 1990, ApJ, 356, 359
Hummer, D. G. & Storey, P. J. 1987, MNRAS, 224, 801
Imanishi, M. & Dudley, C. C. 2000, ApJ, 545, 701
Imanishi, M., Dudley, C. C., Maiolino, R., et al. 2007, ApJS, 171, 72
Imanishi, M., Dudley, C. C., & Maloney, P. R. 2006, ApJ, 637, 114
Iwasawa, K., Matt, G., Guainazzi, M., & Fabian, A. C. 2001, MNRAS, 326, 894
Iwasawa, K., Sanders, D. B., Evans, A. S., et al. 2005, MNRAS, 357, 565
Joseph, R. D. & Wright, G. S. 1985, MNRAS, 214, 87
Krajnović, D., Cappellari, M., de Zeeuw, P. T., & Copin, Y. 2006, MNRAS, 366, 787
Larkin, J. E., Armus, L., Knop, R. A., Matthews, K., & Soifer, B. T. 1995, ApJ, 452, 599
Leitherer, C., Ortiz Otálvaro, P. A., Bresolin, F., et al. 2010, ApJS, 189, 309
Leitherer, C., Schaerer, D., Goldader, J. D., et al. 1999, ApJS, 123, 3
Lonsdale, C. J., Diamond, P. J., Thrall, H., Smith, H. E., & Lonsdale, C. J. 2006, ApJ, 647, 185
Lonsdale, C. J., Lonsdale, C. J., Diamond, P. J., & Smith, H. E. 1998, ApJ, 493, L13
Martin, P. G. & Whittet, D. C. B. 1990, ApJ, 357, 113
Matsushita, S., Iono, D., Petitpas, G. R., et al. 2009, ApJ, 693, 56
McDowell, J. C., Clements, D. L., Lamb, S. A., et al. 2003, ApJ, 591, 154
Mundell, C. G., Ferruit, P., & Pedlar, A. 2001, ApJ, 560, 168
Neumayer, N., Cappellari, M., Reunanen, J., et al. 2007, ApJ, 671, 1329
Norris, R. P. 1988, MNRAS, 230, 345
Papadopoulos, P. P., Isaak, K., & van der Werf, P. 2010a, ApJ, 711, 757
Papadopoulos, P. P., van der Werf, P., Isaak, K., & Xilouris, E. M. 2010b, ApJ, 715, 775
Parra, R., Conway, J. E., Diamond, P. J., et al. 2007, ApJ, 659, 314
Rieke, G. H., Cutri, R. M., Black, J. H., et al. 1985, ApJ, 290, 116
Risaliti, G., Imanishi, M., & Sani, E. 2010, MNRAS, 401, 197
Rodríguez-Rico, C. A., Goss, W. M., Viallefond, F., et al. 2005, ApJ, 633, 198
Rodríguez Zaurín, J., Tadhunter, C. N., & González Delgado, R. M. 2008, MNRAS, 384, 875
Rovilos, E., Diamond, P. J., Lonsdale, C. J., Lonsdale, C. J., & Smith, H. E. 2003, MNRAS, 342, 373
Rovilos, E., Diamond, P. J., Lonsdale, C. J., Smith, H. E., & Lonsdale, C. J. 2005, MNRAS, 359, 827
Sakamoto, K., Scoville, N. Z., Yun, M. S., et al. 1999, ApJ, 514, 68
Sakamoto, K., Wang, J., Wiedner, M. C., et al. 2008, ApJ, 684, 957
Sanders, D. B., Mazzarella, J. M., Kim, D.-C., Surace, J. A., & Soifer, B. T. 2003, AJ, 126, 1607
Scoville, N. Z., Evans, A. S., Dinshaw, N., et al. 1998, ApJ, 492, L107+
Scoville, N. Z., Evans, A. S., Thompson, R., et al. 2000, AJ, 119, 991
Scoville, N. Z., Sargent, A. I., Sanders, D. B., & Soifer, B. T. 1991, ApJ, 366, L5
Scoville, N. Z., Yun, M. S., & Bryant, P. M. 1997, ApJ, 484, 702
Shaya, E. J., Dowling, D. M., Currie, D. G., Faber, S. M., & Groth, E. J. 1994, AJ, 107, 1675
Shioya, Y., Taniguchi, Y., & Trentham, N. 2001a, MNRAS, 321, 11
Shioya, Y., Trentham, N., & Taniguchi, Y. 2001b, ApJ, 548, L29
Smith, H. E., Lonsdale, C. J., Lonsdale, C. J., & Diamond, P. J. 1998, ApJ, 493, L17
Soifer, B. T., Neugebauer, G., Helou, G., et al. 1984, ApJ, 283, L1
Soifer, B. T., Neugebauer, G., Matthews, K., et al. 1999, ApJ, 513, 207
Solomon, P. M., Radford, S. J. E., & Downes, D. 1990, ApJ, 348, L53
Spoon, H. W. W., Marshall, J. A., Houck, J. R., et al. 2007, ApJ, 654, L49
Spoon, H. W. W., Moorwood, A. F. M., Lutz, D., et al. 2004, A&A, 414, 873
Tacconi, L. J., Genzel, R., Lutz, D., et al. 2002, ApJ, 580, 73
van der Hulst, J. M., Terlouw, J. P., Begeman, K. G., Zwitser, W., & Roelfsema, P. R. 1992, in Astronomical Society of the Pacific Conference Series, Vol. 25, Astronomical Data Analysis Software and Systems I, ed. D. M. Worrall, C. Biemesderfer, & J. Barnes, 131–+

van der Werf, P. P. 2001, in Starburst galaxies: near and far, 151

Vázquez, G. A. & Leitherer, C. 2005, ApJ, 621, 695

Vogelaar, M. G. R. & Terlouw, J. P. 2001, in Astronomical Society of the Pacific Conference Series, Vol. 238, Astronomical Data Analysis Software and Systems X, ed. F. R. Harnden Jr., F. A. Primini, & H. E. Payne, 358–+

Wilson, C. D., Harris, W. E., Longden, R., & Scoville, N. Z. 2006, ApJ, 641, 763

Zhao, J.-H., Anantharamaiah, K. R., Goss, W. M., & Viallefond, F. 1996, ApJ, 472, 54